Dalton Transactions

ROYAL SOCIETY OF CHEMISTRY

PAPER

View Article Online
View Journal | View Issue

Cite this: *Dalton Trans.*, 2020, **49**, 4323

Single crystal neutron and magnetic measurements of $Rb_2Mn_3(VO_4)_2CO_3$ and $K_2Co_3(VO_4)_2CO_3$ with mixed honeycomb and triangular magnetic lattices†

Tiffany M. Smith Pellizzeri, [a,b] Liurukara D. Sanjeewa,[c] Steven Pellizzeri,[a,b] Colin D. McMillen, [a] V. Ovidiu Garlea,[d] Feng Ye,[d] Athena S. Sefat[c] and Joseph W. Kolis *[a]

Received 19th August 2019,
Accepted 6th December 2019

DOI: 10.1039/c9dt03389k

rsc.li/dalton

Two new alkali vanadate carbonates with divalent transition metals have been synthesized as large single crystals *via* a high-temperature (600 °C) hydrothermal technique. Compound **I**, $Rb_2Mn_3(VO_4)_2CO_3$, crystallizes in the trigonal crystal system in the space group $P\bar{3}1c$, and compound **II**, $K_2Co_3(VO_4)_2CO_3$, crystallizes in the hexagonal space group $P6_3/m$. Both structures contain honeycomb layers and triangular lattices made from edge-sharing MO_6 octahedra and MO_5 trigonal bipyramids, respectively. The honeycomb and triangular layers are connected along the *c*-axis through tetrahedral [VO_4] groups. The MO_5 units are connected with each other by carbonate groups in the *ab*-plane by forming a triangular magnetic lattice. The difference in space groups between **I** and **II** was also investigated with Density Functional Theory (DFT) calculations. Single crystal magnetic characterization of **I** indicates three magnetic transitions at 77 K, 2.3 K, and 1.5 K. The corresponding magnetic structures for each magnetic transition of **I** were determined using single crystal neutron diffraction. At 77 K the compound orders in the MnO_6-honeycomb layer in a Néel-type antiferromagnetic orientation while the MnO_5 triangular lattice ordered below 2.3 K in a colinear 'up–up–down' fashion, followed by a planar 'Y' type magnetic structure. $K_2Co_3(VO_4)_2CO_3$ (**II**) exhibits a canted antiferromagnetic ordering below T_N = 8 K. The Curie–Weiss fit (200–350 K) gives a Curie–Weiss temperature of −42 K suggesting a dominant antiferromagnetic coupling in the Co^{2+} magnetic sublattices.

1. Introduction

Vanadates are some of the most versatile building blocks for new metal oxides due to their ability to adopt many different coordination geometries and oxidation states,[1–4] and can be magnetically active or magnetically neutral.[5–8] In particular, the simple tetrahedral vanadate, $(VO_4)^{3-}$, is an excellent structural building block with other magnetically interesting elements (such as $Mn^{2+/3+}$, Co^{2+}, $Fe^{2+/3+}$). The presence of a second, open shell transition metal leads to structural diversity, and, potentially new and interesting magnetic structures.[7,9–14]

These materials are traditionally made using traditional high temperature solid-state techniques,[15–18] but these approaches can lead to defect formation in the vanadate lattice. Our group has alternatively turned to using high-temperature (T > 500 °C) hydrothermal synthesis, which has proven to provide good quality single crystals.[7,8,19] Our initial studies used hydroxides as mineralizers, and this provided large, high quality single crystals.[5,7,10] We recently started investigating halide and carbonate brines as mineralizers in order to mimic natural conditions and expand structural diversity.[8,19–24]

One of the first vanadate carbonate crystal structures reported by Yakubovich and coworkers, $K_2Mn_3(VO_4)_2(CO_3)$, has a very intriguing structure and some unusual properties.[25] As part of our program we synthesized this material in high temperature hydrothermal conditions as large (6 mm) high quality

[a]*Department of Chemistry and Center for Optical Materials Science and Engineering Technologies (COMSET), Clemson University, Clemson, SC 29634-0973, USA. E-mail: kjoseph@clemson.edu; Fax: +1 864-656-6613; Tel: +1 864-656-4739*
[b]*Department of Chemistry and Biochemistry, Eastern Illinois University, Charleston, IL 61920, USA*
[c]*Materials Science and Technology Division, Oak Ridge National Laboratory, Oak Ridge, Tennessee 37831, USA*
[d]*Neutron Scattering Division, Oak Ridge National Laboratory, Oak Ridge, Tennessee 37831, USA*

†Electronic supplementary information (ESI) available: Structural data in CIF format, PXRD patterns, bond valence sums. CCDC 1943258 and 1943259. For ESI and crystallographic data in CIF or other electronic format see DOI: 10.1039/c9dt03389k

single crystals and subjected it to detailed magnetic and single crystal neutron studies. It displayed some very exotic magnetic properties due to the structure having an alternate honeycomb and triangular Mn^{2+}, S = 5/2 magnetic lattice.[26] The honeycomb layer in $K_2Mn_3(VO_4)_2(CO_3)$ is built from edge sharing MnO_6 octahedra and the triangular layer is built from MnO_5 trigonal bipyramidal units. These MnO_5 units are then linked by carbonate (CO_3^{2-}) units. This could be attributed to a weak field induced transition perpendicular to the *c*-axis and further confirms that the honeycomb and triangular layers are connected *via* tetrahedral vanadate [VO_4^{3-}] units creating multiple magnetic coupling pathways, leading to three distinct magnetic structures.

This interesting behavior prompted us to pursue the preparation of other related metal vanadate carbonates. Herein we report the synthesis, characterization, and magnetism of two transition metal vanadate carbonates. Compound **I**, $Rb_2Mn_3(VO_4)_2CO_3$, is a new structure type with many similar structural features to the parent phase, however, it crystallizes in a trigonal space group, $P\bar{3}1c$. Compound **II**, $K_2Co_3(VO_4)_2CO_3$, crystallizes in the hexagonal space group $P6_3/m$ and is isostructural to the previously reported $K_2Mn_3(VO_4)_2CO_3$ [25] phase. It is of particular interest however since it contains Co^{2+}, which displays anomalously large spin orbit coupling and magnetic moments.[27] Single crystal neutron scattering, oriented magnetic characterization, and Density Functional Theory (DFT) calculations were performed on the structures in this study.

2. Experimental section

2.1. Hydrothermal synthesis of $Rb_2Mn_3(VO_4)_2CO_3$ (I) and $K_2Co_3(VO_4)_2CO_3$ (II)

Synthesis of $Rb_2Mn_3(VO_4)_2CO_3$ (**I**) and $K_2Co_3(VO_4)_2CO_3$ (**II**) single crystals were carried out in 3 × 0.25 inch silver ampoules. The welded ampoules containing reactants (~0.125 g) and mineralizer (0.4 ml) were heated in a counter-pressured Tuttle autoclave at 600 °C for 5 days, at an average pressure of 1.7 kbar. The crystalline products were filtered and washed with deionized water. The chemical reagents used in this study were used as they were received from the supplier: potassium carbonate (Alfa Aesar, 99.997%), rubidium carbonate (Alfa Aesar, 99%), cobalt(II) oxide (Alfa Aesar, 95%), manganese(II) oxide (Strem, 99%), and vanadium(V) oxide (Alfa Aesar, 99.6%).

2.2. Synthesis of $Rb_2Mn_3(VO_4)_2CO_3$ (I)

$Rb_2Mn_3(VO_4)_2CO_3$ (**I**), was prepared from a mixture of manganese(II) oxide (0.035 g, 0.498 mmol) and vanadium(V) oxide (0.091 g, 0.498 mmol) in a 1 : 1 mole ratio with 0.4 mL of 5 M rubidium carbonate mineralizer under the hydrothermal conditions above. Orange and dark red hexagonal plates and columns were isolated as the main phase. Both crystal morphologies were identified as **I** from single-crystal X-ray diffraction.

2.3. Synthesis of $K_2Co_3(VO_4)_2CO_3$ (II)

Single-crystals of $K_2Co_3(VO_4)_2CO_3$ (**II**) were synthesized using the same procedure as (**I**), except cobalt(II) oxide was used in place of manganese(II) oxide and 5 M potassium carbonate was used as the mineralizer. The reaction yielded dark green hexagonal plates as the main phase. These crystals were identified as **II** by single-crystal X-ray diffraction.

2.4. X-Ray diffraction

Well-formed single crystals of $Rb_2Mn_3(VO_4)_2CO_3$ (**I**) and $K_2Co_3(VO_4)_2CO_3$ (**II**) were used to determine the structures of each compound. The data were collected at room temperature utilizing a Bruker D8 Venture Photon 100 single-crystal diffractometer (Mo Kα radiation, λ = 0.71073 Å). The crystal diffraction images were collected using ϕ and ω-scans. The diffractometer was equipped with an Incoatec IμS source using the APEXIII software suite for data set-up, collection, and processing.[28] Both structures were resolved using intrinsic phasing and full-matrix least square methods with refinement on F^2. All of the structure refinements were done using the SHELXTL software suite.[29] All atoms were first refined with isotropic thermal displacement parameters and then they were refined anisotropically. Table 1 provides a summary of the structural refinement data for $Rb_2Mn_3(VO_4)_2CO_3$ (**I**) and $K_2Co_3(VO_4)_2CO_3$ (**II**). Table 2 lists selected interatomic bond lengths and bond angles for both compounds. The divalent oxidation state of Mn and Co in the present compounds was confirmed by bond valence sum analysis (ESI, Table S1†).

In order to investigate the phase-purity, powder X-ray diffraction (PXRD) measurements of the bulk products were done using a Rigaku Ultima IV diffractometer with Cu Kα radiation (λ = 1.5406 Å). The PXRD patterns were taken at a scan speed

Table 1 Structure refinement data for $Rb_2Mn_3(VO_4)_2CO_3$ (I) and $K_2Co_3(VO_4)_2CO_3$ (II)

	$Rb_2Mn_3(VO_4)_2CO_3$ (I)	$K_2Co_3(VO_4)_2CO_3$ (II)
Empirical formula	$Rb_2Mn_3V_2CO_{11}$	$K_2Co_3V_2CO_{11}$
F.W. (g mol^{-1})	625.65	544.88
Temperature (K)	298(2)	298(2)
Crystal system	Trigonal	Hexagonal
Space group	$P\bar{3}1c$ (no. 163)	$P6_3/m$ (no. 176)
a (Å)	5.2488(3)	5.0931(2)
c (Å)	22.7020(14)	22.1551(13)
Volume (Å^3)	541.64(7)	497.70(5)
Z	2	2
D(calcd) (mg m^{-3})	3.836	3.636
Wavelength (Å)	0.71073	0.71073
μ, mm^{-1}	14.042	7.595
F(000)	578	518
Crystal size (mm)	0.22 × 0.18 × 0.08	0.22 × 0.200 × 0.040
θ range, °	3.59° to 28.26°	3.68° to 26.40°
Reflections collected	3863	6141
Independent reflections	453	357
Final R indices	R_1 = 0.0299[a]	R_1 = 0.0327[a]
	wR_2 = 0.0667[b]	wR_2 = 0.0879[b]
R indices (all data)	R_1 = 0.0400[a]	R_1 = 0.0346[a]
	wR_2 = 0.0701[b]	wR_2 = 0.0895[b]
Goodness-of-fit on F^2	1.180	1.127

[a] $R_1 = \sum||F_o| - [F_c||/\sum|F_o|$. [b] $wR_2 = \{\sum[w(F_o^2 - F_c^2)^2]/\sum[wF_o^2]^2\}^{1/2}$.

Table 2 Selected interatomic bond distances (Å) and angles (°) for $Rb_2Mn_3(VO_4)_2CO_3$ (I) and $K_2Co_3(VO_4)_2CO_3$ (II)

$Rb_2Mn_3(VO_4)_2CO_3$ (I)		$K_2Co_3(VO_4)_2CO_3$ (II)	
Mn1–O1 × 3	2.156(3)	Co1–O1 × 3	2.080(2)
Mn1–O1 × 3	2.210(3)	Co1–O1 × 3	2.1083(19)
Mn2–O2 × 2	2.192(5)	Co2–O2 × 2	2.106(4)
Mn2–O3 × 3	2.096(7)	Co2–O3 × 3	2.038(4)
V1–O2 × 1	1.704(5)	V1–O1 × 1	1.7379(19)
V1–O1 × 3	1.733(3)	V1–O1 × 2	1.7380(19)
C1–O3 × 3	1.277(6)	V1–O2 × 1	1.687(5)
		C1–O3	1.279(3)
O1–Mn1–O1	95.49(10)	O1–Co1–O1	93.49(7)
O1–Mn1–O1	172.60(11)	O1–Co1–O1	175.69(7)
O1–Mn1–O1	91.86(10)	O1–Co1–O1	90.72(7)
O2–Mn2–O2	180.0	O2–Co2–O2	180.0
O2–Mn2–O3	89.91(17)	O2–Co2–O3	90.0
O3–Mn2–O3	120.0	O3–Co2–O3	120.0
O3–Mn2–O2	90.09(17)	O3–Co2–O2	90.0
O1–V1–O1	110.08(9)	O2–V1–O1	108.78(7)
O2–V1–O1	108.85(10)	O1–V1–O1	110.15(7)
O3–C1–O3	120.0	O3–C1–O3	120.0
Mn–Mn honeycomb lattice distances		**Co–Co honeycomb lattice distances**	
Mn1–Mn1	3.04(2)	Co1–Co1	2.94(13)
Mn2–Mn2	5.2488(3)	Co2–Co2	5.0931(2)

of 0.5° min^{-1} between 5° to 65° in 2θ at increments of 0.02°. The PXRD patterns of the bulk reaction products in Fig. S1 and S2 of the ESI† compare very favorably with the calculated PXRD patterns of the single crystals, indicating phase purity.

2.5 Computational details

DFT calculations were carried out within the pseudopotential and plane-wave approach using the Quantum ESPRESSO (v 6.3) suite of programs.[30,31] The electron exchange and correlation were calculated using the Perdew–Burke–Ernzerhof (PBE) implementation of the generalized gradient approximation (GGA).[32] All DFT calculations used a combination of ultrasoft (USPP), projector-augmented wave (PAW), and norm-conserving (NC) pseudopotentials as recommended by the SSSP library.[33,34] USPP pseudopotentials with valence configurations of $3s^23p^63d^74s^1$, $3s^23p^63d^54s^{1.5}$, and $3s^23p^63d^34s^2$ were used to describe the Co, Mn, and V atoms, respectively. PAW pseudopotentials with valence configurations of $2s^22p^4$, $2s^22p^2$, $3s^23p^64s^1$ were used to describe the O, C, and K atoms, respectively. Lastly, Rb atoms were described with a NC pseudopotential with a valence configuration of $4s^24p^65s^1$. All simulations used spin polarization. To better account for the electron configurations in the unfilled 3d shells of the Mn, Co, and V atoms, DFT+U corrections were applied[35] with values of U set to 3.90 eV, 3.32 eV, and 3.25 eV for Mn, Co, and V, respectively.[36] A kinetic energy cutoff of 85 Ry was used for the wave functions and a kinetic energy cutoff of 1020 Ry was used for the charge density and potential. Single point energies and geometry optimizations employed a gamma-centered Monkhorst–Pack *k*-point mesh of 5 × 5 × 1 and Gaussian smearing of 0.01 Ry. These parameters were chosen since they produced near identical results to simulations using significantly larger cutoffs (within 0.35 mRy using 100 Ry and 1400 Ry cutoffs for the wavefunctions and charge density, respectively) and denser *k*-point meshes (within 3×10^{-4} mRy with a 9 × 9 × 2 mesh) at a much lower computational cost. The relaxation of the electronic degrees of freedom was stopped when the energy change was smaller than 10^{-8} Ry. The quasi-Newton algorithm was used for geometry optimization, with convergence thresholds on the total energy and forces of 0.1 mRy and 1 mRy $Bohr^{-1}$, respectively.

2.6 Magnetic and neutron studies

Temperature and field dependent magnetic studies were performed using a Quantum Design Magnetic Property Measurement System (MPMS). The measurements were carried out with the crystallographic *c*-axis aligned either parallel or perpendicular to the applied magnetic field. For **I**, a single crystal specimen was used with a weight of 6.16 mg, and for **II**, several aligned single crystals were used. Single crystals were affixed to a fused silica rod using GE varnish and placed inside plastic drinking straws for the measurements. The temperature dependence magnetic susceptibility, χ, was measured over a temperature range of 2 to 300 K for applied fields *H* between 0.005 to 6 T. The isothermal magnetization measurements were performed for fields up to 6 T. Heat-capacity measurements of $Rb_2Mn_3(VO_4)_2(CO_3)$ (**I**) were performed using a Physical Property Measurement System (PPMS, Quantum Design) in zero and 4 T applied magnetic fields parallel to the crystal *c*-axis. For the heat capacity measurement below 2 K, a PPMS ^{3}He insert was used.

Elastic single crystal neutron scattering was performed on **I** down to 1.6 K using the white beam in the CORELLI instrument at the Spallation Neutron Source (SNS).[37] The data were collected in the absence of magnetic field using a single crystal specimen of 1 × 1 × 3 mm^3 dimensions. Data were collected in steps of 3° over a range of 150°. Mantid software was utilized to analyze the scattering data.

3. Results and discussion

3.1. Synthesis of $Rb_2Mn_3(VO_4)_2CO_3$ (I) and $K_2Co_3(VO_4)_2CO_3$ (II)

Through our investigations of transition metal vanadates with various alkali and alkaline earth counter-ions we determined that the mineralizer identity has a significant effect on the final products. We investigated hydroxide, chloride, fluoride, and mixed hydroxide/brine mineralizers, leading to crystal structures that sometimes incorporate the alkali/alkaline earth metal and/or the halide counter-ion.[8,20–22] We recently started to investigate carbonate brines as mineralizers and our initial work led to the synthesis of large high-quality single crystals of $K_2Mn_3(VO_4)_2CO_3$, originally reported by Yakubovich *et al.*[25] The large single crystals enabled the detailed study of its complex magnetic structure. The rich magnetic behavior encouraged us to explore other analogs of this interesting system. As a result, we isolated two new compounds,

$Rb_2Mn_3(VO_4)_2CO_3$ (**I**) and $K_2Co_3(VO_4)_2CO_3$ (**II**), both which contain the carbonate anion within the structural framework.

These materials were both synthesized from a 1 : 1 ratio of manganese(II) oxide (in the case of structure **I**) or cobalt(II) oxide (in the case of **II**) and vanadium(V) oxide in the appropriate 5 M carbonate mineralizer. Structure **I**, $Rb_2Mn_3(VO_4)_2CO_3$, is very similar to $K_2Mn_3(VO_4)_2CO_3$,[25] but the rubidium analog, **I**, crystallizes in a different space group of $P\bar{3}1c$ *versus* $P6_3/m$ for the potassium analog. In contrast, compound **II**, $K_2Co_3(VO_4)_2CO_3$, is completely isostructural to the parent $K_2Mn_3(VO_4)_2CO$.[25] It is of considerable interest however, as it is expected to have very different magnetic properties because of the difference in spin state of the magnetic ion (Co^{2+}, $S = 3/2$ *vs.* Mn^{2+} $S = 5/2$). Additionally, due to the anomalously large spin–orbit interaction well known in Co^{2+} ions, the effective spin of Co^{2+} can also be represented by $S = \frac{1}{2}$.[27] The presence of the low effective spin is expected to markedly enhance the quantum fluctuation and trigger exotic quantum states in $K_2Co_3(VO_4)_2CO_3$.[38,39]

Both $Rb_2Mn_3(VO_4)_2CO_3$ (**I**) and $K_2Co_3(VO_4)_2CO_3$ (**II**), as well as the $K_2Mn_3(VO_4)_2CO_3$ compound all grow as large single crystals (Fig. 1), with an average size of about 2 mm in the longest direction. Interestingly, in both cases we start with divalent metal oxides and vanadium(V) oxide as the starting materials so we observe no oxidation or reduction of the starting materials in the course of the reaction.

Fig. 1 Optical micrograph of $K_2Mn_3(VO_4)_2CO_3$, $Rb_2Mn_3(VO_4)_2CO_3$ (**I**), and $K_2Co_3(VO_4)_2CO_3$ (**II**). For scale, the center crystal is about 1 mm across in width.

3.2. Crystal structures of $Rb_2Mn_3(VO_4)_2CO_3$ (I) and $K_2Co_3(VO_4)_2CO_3$ (II)

The structural aspects of these two compounds are reviewed in some detail here because of their importance in the interpretation of the magnetic and neutron scattering data (see below). Compound **I** crystallizes in the trigonal space group $P\bar{3}1c$ and is a three-dimensional structure built from two separate layers coordinated to one another by $[VO_4]$ tetrahedra. One layer contains a honeycomb arrangement of $[MnO_6]$ octahedra, and the other consists of trigonal bipyramidal $[MnO_5]$ units and a planar triangular arrangement of $[CO_3]$ groups. Fig. 2 displays a view in the *ab*-plane of the Mn–O–Mn honeycomb layer (left) and manganese carbonate triangular layer (right) with the manganese metal centers connected by thick yellow lines to show the honeycomb and triangular arrangements in the octahedral manganese layer and the manganese carbonate triangular layer, respectively.

The manganese(II) honeycomb layer and triangular layer in $Rb_2Mn_3(VO_4)_2CO_3$ (**I**) each only contain one unique manganese atom. The Mn1 ion is octahedral in geometry and sits at the 4*f* Wyckoff site. At all of its vertices Mn1 coordinates to symmetry equivalent O1 atoms, which in turn creates edge-sharing interactions between the MnO_6 atoms. The vanadium atom, V1, sits at the 4*e* Wyckoff site and is coordinated to O1 at three of its vertices with corner-sharing to Mn1, to provide connectivity of the honeycomb manganese layer (through O1) to the manganese carbonate triangular layer (through O2).

The second unique divalent manganese ion, Mn2, sits at the 2*a* Wyckoff site and is 5-coordinate trigonal bipyramidal in its geometry. It is bound to O2 at its two axial positions through corner-sharing with V1, and at is three equatorial positions it coordinates to three symmetry equivalent O3 atoms. This generates a corner-sharing interaction between Mn1 and the carbonate group, forming the $[MnCO_3]$ layer. The tetrahedral $[VO_4]$ group coordinates the manganese carbonate triangular layer and the honeycomb manganese layer together by corner-sharing to form a three-dimensional structure. The average Mn–O bond distance in **I** is 2.161(7) Å, which is in the range to be expected for Mn^{2+}. The average V–O bond distance is 1.726(5) Å, appropriate for vanadium (5+) tetrahedra.

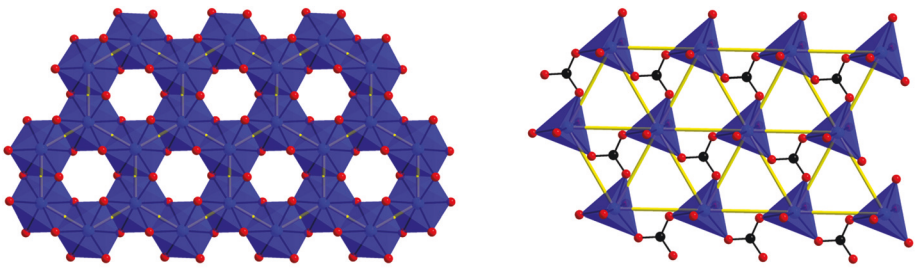

Fig. 2 View on the *ab* plane of the Mn–O–Mn layer (left) and manganese carbonate trigonal bipyramidal layer (right) in $Rb_2Mn_3(VO_4)_2CO_3$ (**I**). Manganese atoms are drawn connected to one another to display the hexagonal and triangular arrangements between the metal centers. Color scheme: blue polyhedra (manganese), red spheres (oxygen), black spheres (carbon).

The other polymorphs of this class, $K_2Co_3(VO_4)_2CO_3$ (**II**) and the parent $K_2Mn_3(VO_4)_2CO_3$, crystallize in the hexagonal space group $P6_3/m$. Initially we tried solving structure **I** in $P6_3/m$, however, we could not reach a reasonable structure solution, whereas the trigonal solution was clearly the correct one. The major difference can be seen in viewing structures **I** and **II** side by side (Fig. 3). The vanadate tetrahedra along the *bc*-plane from left to right in $Rb_2Mn_3(VO_4)_2CO_3$ (**I**), are in the "up, down, up, down" pattern. The $[VO_4]$ tetrahedra in **II** however, are in the "up, up, down, down" pattern. This subtle change in the vanadate tetrahedra, and, presumably, the increase in cation size from potassium to rubidium, leads to the different space groups for **I** and **II**. A further consequence of the space group difference is that the carbonate group of **I** is disordered (Fig. 4), with the O3 atom of the carbonate group half-occupied at a general position. Since O3 is also bound to the alkali metals in the structure, we presume the identity and size of the alkali metal are influential. However, neither the vanadate orientation nor the carbonate disorder influence the arrangement of the magnetically-active Mn sites relative to one another. To further investigate the differences in space group between these compounds, we performed Density Functional Theory (DFT) calculations (see section 3.3).

The Mn–O octahedra bond lengths in **I** range from 2.156(3) Å to 2.210(3) Å, whereas the Mn–O octahedra bond distances in the original $K_2Mn_3(VO_4)_2CO_3$ are slightly shorter in length, ranging from 2.144(1) Å to 2.195(1) Å. The 5-coordinate Mn–O bond lengths in **I** range from 2.096(7) Å to 2.192(5) Å, whereas the 5-coordinate Mn–O bond lengths in $K_2Mn_3(VO_4)_2CO_3$ have a smaller range from 2.124(2) Å to 2.151(2) Å. Additionally, it is interesting to compare the Mn–Mn bond distances in the honeycomb and triangular layers for both **I** and $K_2Mn_3(VO_4)_2CO_3$. The Mn–Mn honeycomb distance in **I** is 3.0370(2) Å, whereas the Mn–Mn honeycomb distance in $K_2Mn_3(VO_4)_2CO_3$ is shorter at 3.01 Å. The same trend is seen in comparing the Mn–Mn bond distances in the triangular layer, the Mn–Mn distance in **I** is 5.249 Å, whereas the Mn–Mn distance in $K_2Mn_3(VO_4)_2CO_3$ is 5.201 Å. As expected all distances are slightly longer in $Rb_2Mn_3(VO_4)_2CO_3$ compared to $K_2Mn_3(VO_4)_2CO_3$, so we expect the magnetic ordering temperatures in the honeycomb and triangular lattice of **I** to also be slightly different compared to the published $K_2Mn_3(VO_4)_2CO_3$.

Compound **II** is rigorously isostructural to the parent $K_2Mn_3(VO_4)_2CO_3$, with two unique Co^{2+} atoms, one in the cobalt honeycomb layer and one in the cobalt carbonate triangular layer. Additionally, there is one unique vanadium site, V1, which sits on the 4*e* Wyckoff site, and connects the honeycomb layer to the carbonate triangular layer. The octahedral cobalt atom that is a part of the cobalt vanadate layer, Co1, sits on the 4*f* Wyckoff site and coordinates to symmetry equivalent O1 atoms at all of its vertices, and provides an edge-sharing interaction between Co1 atoms forming the honeycomb layer.

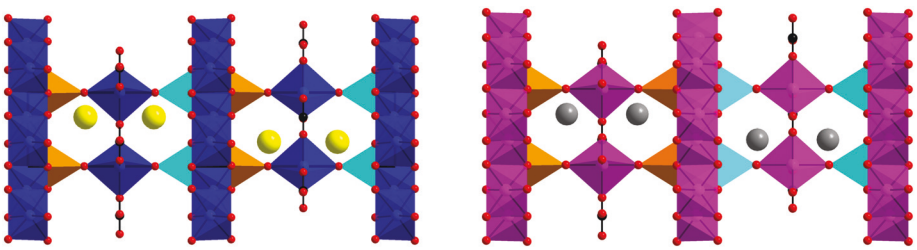

Fig. 3 Comparison of $Rb_2Mn_3(VO_4)_2CO_3$ (**I**) (left) and $K_2Co_3(VO_4)_2CO_3$ (**II**) (right) in the *bc* plane. Color scheme: Potassium (grey spheres), rubidium (large yellow spheres), cobalt (purple polyhedra), manganese (blue polyhedra), vanadium (orange and cyan tetrahedra), oxygen (small red spheres), and carbon (small black spheres). The orange and cyan colors used for the vanadate tetrahedra distinguish two different orientations of the vanadate oxyanions.

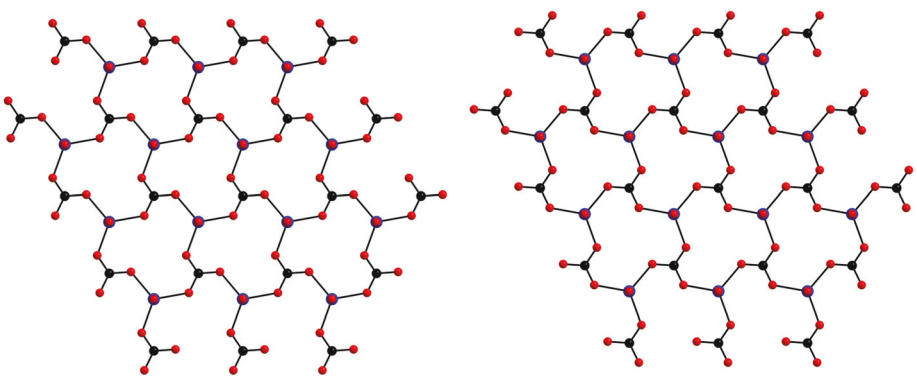

Fig. 4 Two disordered orientations of the carbonate groups in the layer containing the trigonal bipyramidal Mn sites in **I**.

This vanadate also connects to the cobalt carbonate triangular layer through corner sharing.

The Co1–O1 bond distances range from 2.080(2) Å to 2.1083 (19) Å, with three longer bond lengths leading to a distorted octahedral geometry for Co1. This distortion can be seen clearly from the Co1–Co1 distances between edge-shared units. The Co1–Co1 distance is 2.9430(1) Å in **II** (with a Co1–O1–Co1 angle of 87.15(10)° to 93.49(7)°), whereas the Mn1–Mn1 distance in **I** is 3.0370(2) Å (with a Mn1–O1–Mn1 angle of 84.64 (16)° to 95.49(10)°).

The other cobalt atom, Co2, in the carbonate-containing triangular layer, sits on the 2*a* Wyckoff site. At its three symmetry equivalent equatorial O3 positions, the cobalt atom coordinates to the carbonate group through corner-sharing. It is coordinated to the honeycomb layer through O2 in the $[VO_4]$ group. The Co2–O bonds range from 2.038(4) Å to 2.106(4) Å, with the three equatorial bonds at the shorter 2.038(4) Å distance, and the two axial bonds at the longer distance. The Co–Co distance in the triangular carbonate triangular layer is 5.09 Å, which is much larger than the honeycomb layer because the Co2 atoms are connected through carbonate groups, as opposed to edge-sharing with one another. The Mn2–Mn2 bond distances in **I** are slightly longer at 5.25 Å. It is also interesting to note that the C1–O3–Co2 bond angle in **II** is 123.2(2)°, whereas the C1–O3–Mn2 bond angle in **I** is slightly more obtuse at 126.2(5)°. It is also interesting to note that the space between the cobalt carbonate triangular layer and the cobalt honeycomb layer is 5.6 Å, while the space between the layers in **I** is slightly longer at 5.8 Å. All of these factors lead to the subtle difference in structure and symmetry of **I** as compared to **II**. The average V–O bond length at 1.725(4) Å is in the range to be expected for V^{5+}. Fig. 5 displays the cobalt vanadate layer (left) and cobalt carbonate triangular layer (right) in the *ab* plane, with the honeycomb and triangular arrangements of the cobalt ions highlighted with a thick yellow line.

3.3 Density functional theory (DFT) calculations

Periodic DFT calculations were performed to compare the electronic differences between both the $P\bar{3}1c$ and $P6_3/m$ space group settings for both $Rb_2Mn_3(VO_4)_2CO_3$ (**I**) and $K_2Co_3(VO_4)_2CO_3$ (**II**). The O3 atom bound to C1 to form the carbonate anion was found to be half occupied in the $P\bar{3}1c$ space group setting. Therefore, the atomic positions form the crystallographic solution could not be directly used in the simulation. To produce a set of atomic positions in which all atoms are fully occupied, the software Supercell[40] was used to produce possible configurations that would fulfill this requirement. This analysis resulted in a total of 90 unique combinations after removing symmetrically equivalent possibilities. A combination of Ewald summation and visual inspection was used to identify two configurations that corresponded to both orientations of the carbonate anion in the $P\bar{3}1c$ space group setting. For the comparison of the energy differences, the energies of these two configurations were averaged, while for the comparison of the geometry optimizations these configurations were treated separately.

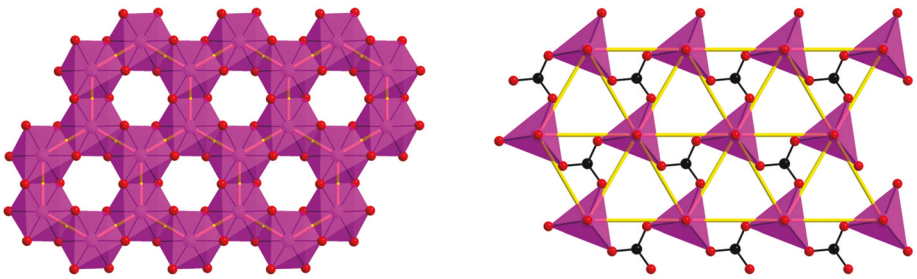

Fig. 5 View on the *ab* plane of the Co–O–Co layer (left) and cobalt carbonate triangular layer (right) in $K_2Co_3(VO_4)_2CO_3$ (**II**). Cobalt atoms are drawn connected to one another to display the hexagonal and triangular arrangements between the metal centers. Color scheme is the same as Fig. 3.

Table 3 Comparison of average interatomic bond distances (Å) for $Rb_2Mn_3(VO_4)_2CO_3$ (I) and $K_2Co_3(VO_4)_2CO_3$ (II) with the experimentally determined atomic positions from the $P6_3/m$ and $P\bar{3}1c$ space group settings and computational optimized atomic positions. Additionally, calculated root mean squared derivations (RMSD) (Å) and mean absolute error (MAE) (Å) are provided

$Rb_2Mn_3(VO_4)_2CO_3$ (**I**)				$K_2Co_3(VO_4)_2CO_3$ (**II**)			
	$P6_3/m$	$P\bar{3}1c$	Calc.		$P6_3/m$	$P\bar{3}1c$	Calc.
Rb–O	2.932	2.935	2.935	K–O	2.856	2.812	2.849
Mn1–O	2.186	2.183	2.195	Co1–O	2.094	2.139	2.099
Mn2–O	2.365	2.134	2.151	Co2–O	2.065	2.052	2.053
V–O	1.720	1.726	1.730	V–O	1.725	1.688	1.730
C–O	1.180	1.277	1.293	C–O	1.279	1.330	1.292
RMSD	0.2422	**0.0263**		RMSD	**0.0204**	0.0790	
MAE	0.0699	**0.0098**		MAE	**0.0084**	0.0317	

Using the atomic positions determined through the X-ray structure refinements, the total energy differences for both compounds were compared in the $P\bar{3}1c$ and $P6_3/m$ space groups for both compounds. For **I**, the $P\bar{3}1c$ space group setting was more energetically favored by 4.276 eV in comparison to the $P6_3/m$ space group setting. In contrast, the $P6_3/m$ space group setting for **II** was more energetically favored by 0.648 eV compared to the $P\bar{3}1c$ space group setting. These results agree with the preferred space group settings from the structural refinements.

In efforts to explain the large energetic difference between the two space group settings for **I**, bonding distances of each structure were compared. For **I**, it was found that the bond distance between C1–O3 calculated in the $P6_3/m$ setting (1.18 Å) was abnormally small as compared to the $P\bar{3}1c$ (1.277 Å) space group setting, which likely resulted in this large energy difference due to increased nuclear repulsion between C1–O3 in the $P6_3/m$ setting. In contrast for **II**, the difference in this bond length is much smaller with values of 1.279 Å and 1.33 Å for the $P6_3/m$ and $P\bar{3}1c$ space group setting, respectively. In both **I** and **II** this C1–O3 bond length deviated from the ideal bond length of a carbonate ion, which could be one explanation for the space group preferences of **I** and **II**.

In addition to the calulation of the energetics of the two space group settings using atomic positions fixed at their crystallographically determined positions, the atomic positions were allowed to relax while keeping the crystallographically determined lattice parameters fixed. This produced nearly identical electronic energies (<0.003 eV), irrespective of the starting configuration. To determine which of the experimentally determined structures was the most similar to the computationally optimized geometry the bond-lengths were compared. Table 3 shows the average bond lengths, the calculated root mean squared derivations (RMSD) and mean absolute error (MAE) of the crystallographically determined bond lengths compared to the average of the computationally derived bond lengths.

The calculated bond lengths for $Rb_2Mn_3(VO_4)_2CO_3$ (**I**) were found to more closely match those for the $P\bar{3}1c$ space group setting of **I** with an RMSD of 0.0263 Å as compared to the $P6_3/m$ setting, which had an RMSD of 0.2422 Å. This is consistent with the experimentally determined space group setting for **I**. The average values for the Rb–O, Mn1–O, and the V–O bonds are very similar in all three cases. The main differences are primarily in the bond lengths for Mn2–O and the C–O bonds. The computationally optimized structure favors the observed $P\bar{3}1c$ space group setting, in that it shows a shorter bond length for the Mn2–O bonds and the longer bond length for C–O, compared to the $P6_3/m$ setting of **I**. By comparison, the calculated bond lengths for $K_2Co_3(VO_4)_2CO_3$ (**II**) favored the $P6_3/m$ space group setting of **II** with an RMSD of 0.0204 Å as compared to the $P\bar{3}1c$ setting which had an RMSD of 0.0790 Å. In this case the average values for the K–O, Co2–O, and the C–O bonds are very similar in all three cases, while the main differences are in the bond lengths for the Co1–O and V–O bonds. The computationally optimized structure predicts bond lengths in line with those determined using the $P6_3/m$ space group setting in that it shows a shorter bond length for the Co1–O bonds and the longer bond length for V–O as compared to the $P\bar{3}1c$ setting of **II**. Overall, the unfavorable space group

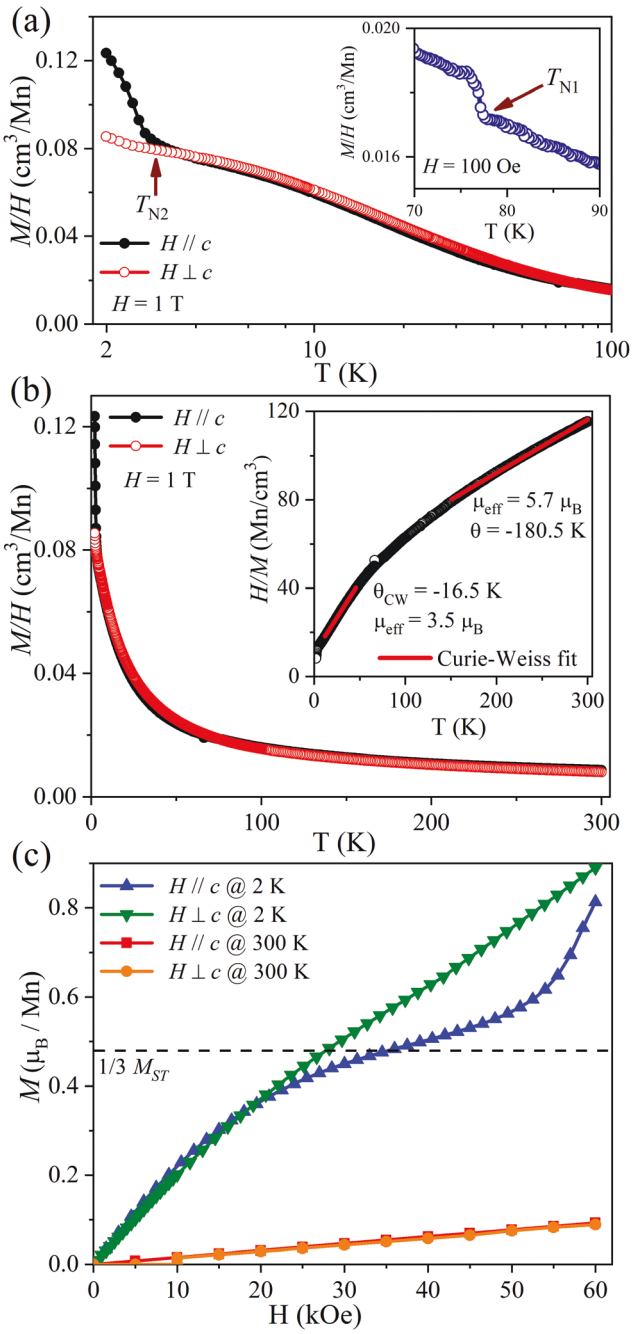

Fig. 6 Susceptibility and magnetization data of $Rb_2Mn_3(VO_4)CO_3$ (I) with applied magnetic field parallel and perpendicular to *c*-axis. (a) Magnetic susceptibility at 1 T applied magnetic field (2–300 K) and Curie–Weiss fits in two different temperature ranges are displaying in the inset. (b) Enlarge view of susceptibility data between 100–2 K and inset shows the magnetic susceptibility data at 100 Oe applied magnetic field *H*//*c*-axis where a kink was observed at 78 K (T_{N1}). (c) Isothermal magnetization data obtained at 2 and 300 K. The dashed line indicates the 1/3 magnetic saturation (1/3 M_{ST}) of the triangular lattice.

settings result in structures that distort the bond lengths, resulting in energetic penalties for these configurations.

3.4 Magnetization and neutron studies of $Rb_2Mn_3(VO_4)_2CO_3$ (I)

The temperature dependent magnetic susceptibility of $Rb_2Mn_3(VO_4)_2CO_3$ (**I**) with the magnetic field parallel and perpendicular to the *c*-axis is summarized in Fig. 6. The magnetic properties of $Rb_2Mn_3(VO_4)_2CO_3$ (**I**) are very similar to the previously reported $K_2Mn_3(VO_4)_2CO_3$ which was characterized in detail using elastic and inelastic neutron scattering techniques.[26] $Rb_2Mn_3(VO_4)_2CO_3$ (**I**) and $K_2Mn_3(VO_4)_2CO_3$ contain similar magnetic sublattices even though they crystallize in different space groups. As in $K_2Mn_3(VO_4)_2CO_3$, **I** exhibits a sequence of three magnetic transitions at 78 K, 2.3 K, and 1.5 K (see heat capacity data, below). The T_{N1} and T_{N2} magnetic transitions can be clearly observed in Fig. 6a where the magnetic susceptibility was plotted in the logarithmic scale *vs.* temperature. Fig. 6a inset displays the magnetic susceptibility in an applied magnetic field of 100 Oe parallel to the *c*-axis, where a small kink was observed at 78 K (T_{N1}). Further, we assigned T_{N2} as the temperature where the susceptibility shows an upturn in $H//c$-axis, 2.3 K, (Fig. 6a) which is further confirmed by the first derivative $d\chi/dT$. This also agrees with the heat capacity data (see below).

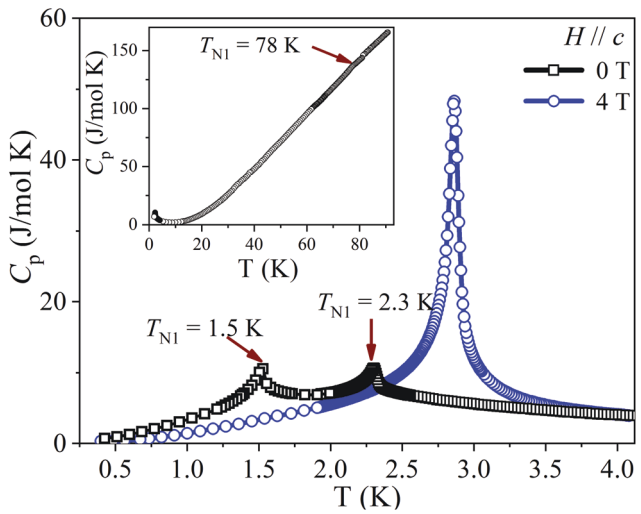

Fig. 7 Heat capacity of $Rb_2Mn_3(VO_4)_2CO_3$ (I) below 4 K with magnetic field along the *c*-axis (H = 0 and 4 T), inset: heat capacity (H = 0 T) from 2–100 K showing a small change in slope at T_{N1} = 78 K.

At two higher temperature regimes (T > 150 K and 10–50 K), the magnetic susceptibility follows a Curie–Weiss law, $\chi = C/(T - \Theta)$, Fig. 6b inset. The best fits for 150–300 K yields C = 4.12 cm^3 per K per mol-Mn and a Weiss temperature of −180.5 K. The large negative Weiss temperature suggests dominant antiferromagnetic interactions in $Rb_2Mn_3(VO_4)_2CO_3$ (**I**). The experimental effective magnetic moment is 5.7μ_B per Mn, which is very close to the spin only value of Mn^{2+}, (S = 5/2, 5.91μ_B), resulting from ordering in the honeycomb layers, similar to what occurs in $K_2Mn_3(VO_4)_2CO_3$.[26] The Curie–Weiss fit of the lower temperature range (10–50 K) resulted in a Weiss temperature of −16.5 K and a Curie constant of C = 1.54 cm^3 per K per mol-Mn and an effective magnetic moment of 3.5μ_B per Mn, which is considerably lower than the expected value for high spin Mn^{2+} (S = 5/2). This behavior was observed in $K_2Mn_3(VO_4)_2CO_3$ as well, and it has been assigned to one third of spin associated in the triangular Mn-lattice made from MnO_5 units, while the other two thirds of the Mn^{2+} spins located in the honeycomb layer are already ordered. The magnetization measurements, $M(H)$, reveal a similar behavior to our previous report,[26] in which the 2 K magnetization measurement parallel to the *c*-axis reaches levels slightly off at 3.5 T before it starts to increase sharply, which resembles the

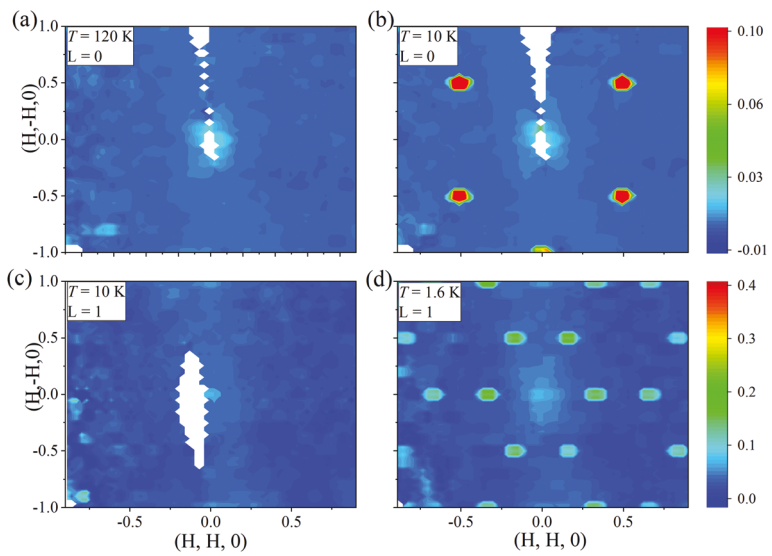

Fig. 8 Data collected at 120 K (a), 10 K (b, c), and 1.6 K (d) using the Corelli instrument that shows the development of (100)-type (HK0 slices) and (1/3,1/3,1)-type (HK1 slices) in magnetic reflections below T_{N1} and T_{N2}, respectively, for compound $Rb_2Mn_3(VO_4)_2CO_3$ (I).

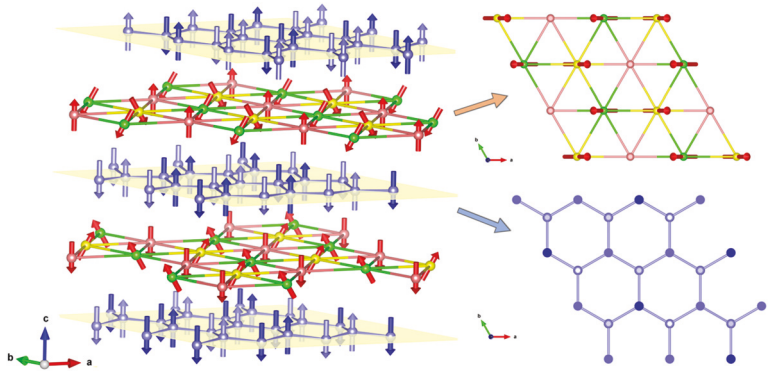

Fig. 9 Schematic magnetic structures of $Rb_2Mn_3(VO_4)_2CO_3$ (I). The blue arrows represent arrangement of Mn(1) spin in the honeycomb layer (4 K < T > 100 K) and red arrows represent the canted Y-type magnetic structure in the triangular lattice made from Mn(2) spins (T < 2 K). The projected view of the magnetic sublattices along the c-axis are displayed in the right panel.

1/3 saturation in the triangular magnetic sub lattice (Fig. 6c). At this point the magnetic moment is ~0.5μ_B per Mn. This is similar to $K_2Mn_3(VO_4)_2CO_3$ which reaches to the first magnetic plateau at about 4.5 T with a magnetic moment of 0.55μ_B per Mn. Heat capacity measurements were performed on **I** down to 0.4 K to identify both T_{N2} and T_{N3}, which clearly exhibits lambda-shaped peaks at 2.3 K and 1.5 K for T_{N2} and T_{N3}, respectively (Fig. 7). It is worth mentioning that both T_{N2} and T_{N3} in $Rb_2Mn_3(VO_4)_2CO_3$ are lower than those reported (3 K and 2 K) for $K_2Mn_3(VO_4)_2CO_3$.[25] These subtle differences could be due to the minor structural differences associated in the bond distances and angles in the rubidium and potassium structures, where the MnO_5 units are slightly more distorted and the distance between MnO_5 units in the triangular lattice is 5.2488(3) Å in **I** compared to 5.201 Å in $K_2Mn_3(VO_4)_2CO_3$.

The magnetic structure was determined using single crystal neutron diffraction. Fig. 8a and b show a comparison of the (HK0) slice data measured at 120 K and 10 K, indicating the appearance of (100)-type magnetic reflections below T_{N1}, while Fig. 8c and d illustrate the magnetic peaks of (1/3,1/3,1)-type in (HK1) slice data collected at 1.6 K. Fig. 9 displays the magnetic structures of $Rb_2Mn_3(VO_4)CO_3$ (**I**). As observed in $K_2Mn_3(VO_4)_2CO_3$, the magnetic structure below 120 K and above 10 K can be best indexed using the magnetic propagation vector $\boldsymbol{k_1}$ = (0 0 0). The determined magnetic structure of the honeycomb layer has Mn spins antiparallel to each other in the *ab*-plane (Fig. 9). The antiferromagnetic honeycomb layers stack ferromagnetically along the *c*-axis. The temperature dependence of the (102) peak intensity marks the magnetic transition associated with T_{N1} = 77 K (Fig. 10a). To determine the magnetic order associated with the triangular layer we collected data at 1.6 K. Here a new set of magnetic peaks appeared which can be indexed using the propagation vector of $\boldsymbol{k_2}$ = (1/3 1/3 0). We observe a collinear magnetic structure for the triangular Mn lattice where Mn spins arrange in an amplitude modulated 'up–up–down' (uud) fashion along the *c*-axis with subsequent magnetic sublattices arranged in an antiferromagnetic (AFM) fashion (Fig. 9). At $T < T_{N3}$ Mn spins

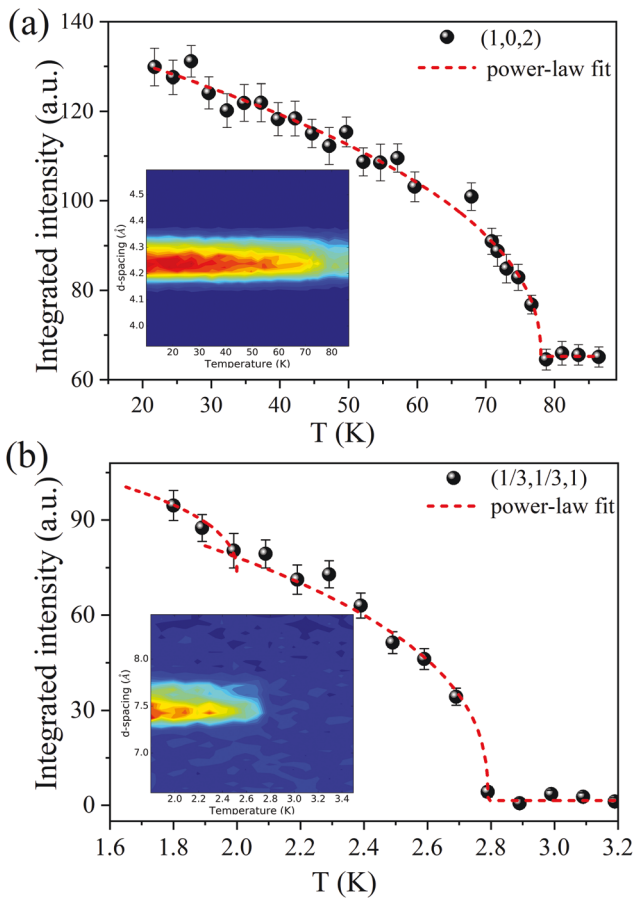

Fig. 10 Temperature dependence of the (1,0,2) (a) and (1/3,1/3,1) (b) magnetic peaks for $Rb_2Mn_3(VO_4)_2CO_3$ (I). The dashed line is a guide to the eye of the order parameter, marking the sequential transition temperatures described in the text. The insets show the color contours of the magnetic peaks.

in the triangular magnetic lattice rearranged from uud to a canted planar structure where moments are rotated in the *ac*-plane by 120° between neighboring spins (Fig. 9). Again, adja-

cent layers remain antiferromagnetic. Further, order parameters of this magnetic reflection were monitored for temperature range 3.5 > T_{N2} (K) > 1.6 K (Fig. 10b). The two magnetic sublattices can be described in *P*6′3/*m* and *P*2′1 magnetic space groups, respectively. This low temperature ordering behavior is generally similar to that observed in the parent $K_2Mn_3(VO_4)_2CO_3$.[26]

3.5 Magnetic properties of $K_2Co_3(VO_4)_2CO_3$ (II)

Magnetic transitions at lower temperature were investigated for **II** as a function of applied magnetic field from 50 Oe to 6 T parallel and perpendicular to the *c*-axis and are considerably different from that of the Mn^{2+} analogs as might be expected. The magnetic properties of $K_2Co_3(VO_4)_2CO_3$ (**II**) clearly exhibit a strong magnetic anisotropy but also display two regions of linear Curie Weiss behavior. The temperature dependent reciprocal magnetic susceptibility of $K_2Co_3(VO_4)_2CO_3$ (**II**) perpendicular to the *c*-axis in applied magnetic field of 1 T can be fitted to the Curie–Weiss law (Fig. 11a). The data fitted from 200–350 K resulted in C = 3.2 cm^3 per K per mol-Co and θ = −45 K. The negative Curie–Weiss temperature suggests a dominant antiferromagnetic interaction in the Co-magnetic lattices, while the effective magnetic moment is 5.06μ_B per Co. Linear fitting from 2–15 K yields C = 1.7 cm^3 per K per mol-Co and θ = −28 K. The obtained effective magnetic moment is 3.7μ_B per Co. The existence of two Curie–Weiss regimes could be associated with the presence of two nearly independent magnetic sublattices formed by honeycomb and triangular layers, respectively. The observation of an effective magnetic moment higher than the theoretical spin only value (Co^{2+} S = 3/2, 3.8μ_B) at higher temperatures could be attributed to the orbital contribution of Co^{2+} in an octahedral environment, a phenomenon well known for Co^{2+}.[27] Moreover, the effective spin Hamiltonian for a distorted octahedral Co^{2+} in the ground state is a Kramers doublet[41,42] such that at lower temperatures Co^{2+} could possess an effective $S = \frac{1}{2}$ state with a g value considerably larger than 2. This behavior has been observed in triangular antiferromagnetic lattices with Co^{2+} in an octahedral environment. For example, the $A_4CoB_2O_{12}$ (A = Ba, Sr, La, B = W, Re) series reported by Rawl *et al.* in 2017 displays a large deviation of g values (3.2–4.2)[43] depending upon the structure. Moreover, in $A_4CoB_2O_{12}$ a spin state crossover was observed

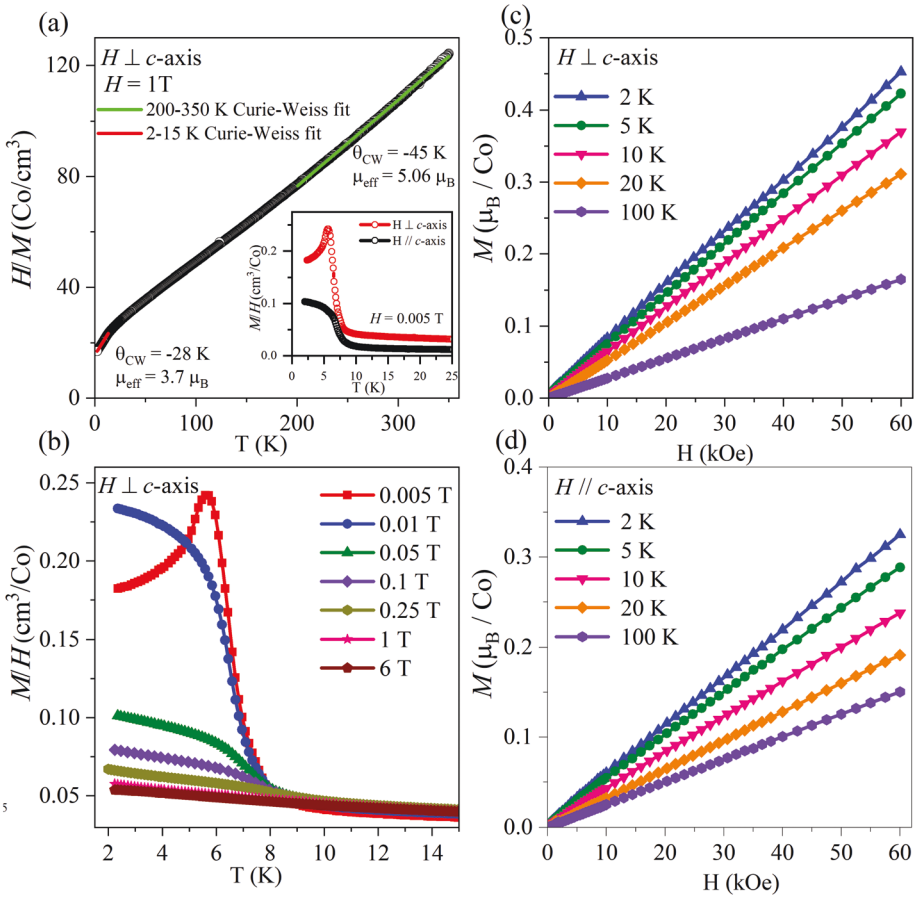

Fig. 11 (a) Inverse susceptibility as a function of temperature. The Curie–Weiss fits are denoted by solid red and green lines for the two different temperature regions. Inset: Magnetic susceptibility obtained in the field cooling mode in the applied magnetic field of 50 Oe parallel and perpendicular to the *c*-axis. (b) Magnetic susceptibility as a function of the applied magnetic fields from 0.005 to 6 T showed the canted antiferrromagnetic nature of $K_2Co_3(VO_4)_2CO_3$ (**II**). (c) and (d) Isothermal magnetization obatined in perpenicular and parallel to the *c*-axis.

from high spin Co^{2+} $S = 3/2$ to low spin Co^{2+} $S = \frac{1}{2}$ with lowering temperature. This is governed by the crystal field splitting and spin orbital coupling which leads to a Kramers doublet ground state at lower temperatures with effective spin $\frac{1}{2}$.[43,44]

The inset of Fig. 11a indicates the highly anisotropic nature of $K_2Co_3(VO_4)_2CO_3$ (**II**). The magnetic susceptibility rises very sharply when the applied magnetic field is perpendicular to the *c*-axis ($H < 1$ T) at around 8 K. The magnetic susceptibility H (50 Oe) $\perp$ *c*-axis reaches a maximum at ~8 K, before it starts to decrease with lowering temperatures compared to H (50 Oe)//*c*-axis. In addition to these key features, we also observed a bifurcation of FC and ZFC below 8 K in the magnetic susceptibility obtained at 50 Oe applied magnetic field. The susceptibility measured in different applied magnetic fields (Fig. 11b) showed that with increasing field, the magnetic phase transition shifts to the lower temperature, which suggests a spin canting behavior in $K_2Co_3(VO_4)_2CO_3$ (**II**).[45] The gradual development of the field induced canting behavior of the Co^{2+} spins can be also observed in the field dependent magnetic susceptibility from 0–6 T (Fig. 11b). The magnetic anisotropy was further confirmed by the isothermal magnetization curves which are presented in Fig. 11b and c. The magnetization curves were obtained between 0–6 T at the temperatures of 2, 5, 10, 20, and 100 K. The magnetization data shows no sign of hysteresis and no saturation up to 6 T. From the magnetization behavior along the two different directions we can conclude that magnetic spins are perpendicular to the *c*-axis which could be the easy-plane 120° arrangement. In the isothermal magnetization measurements, the applied field perpendicular to the *c*-axis it reaches ~0.45μ_B while the applied magnetic field parallel to *c*-axis reaches ~0.3μ_B. In both cases the values are much smaller than the ideal saturated magnetization of Co^{2+}. The isothermal magnetic measurements at 2 and 5 K perpendicular to the *c*-axis show a slight deviation from linear behavior. This could be attributed to a weak field induced transition perpendicular to the *c*-axis and further confirms the easy plane anisotropy in **II**. We expect the Co^{2+}-honeycomb magnetic lattices to order at ~8 K and the Co^{2+}-triangular magnetic lattice to order below 2 K but the magnetic structure should be very complicated since **II** possesses two magnetic sublattices made from six coordinated Co(1) and five coordinated Co(2). Detailed magnetic and neutron diffraction experiments of $K_2Co_3(VO_4)_2CO_3$ (**II**) are currently underway to shed light on these magnetic structures and will be the subject of an upcoming publication.

4. Conclusions

Herein we report the synthesis, structure, and magnetism of two new metal(II) vanadate carbonates, $Rb_2Mn_3(VO_4)_2CO_3$ (**I**) and $K_2Co_3(VO_4)_2CO_3$ (**II**). Each compound contains two distinct layers, one with a trigonal bipyramidal coordinated metal (II) center built from carbonate ions. This layer is coordinated to a second honeycomb layer built from edge-shared octahedra of metal(II). The two layers are connected by [VO_4] groups and each layer possesses trigonal symmetry. The two compounds are structurally similar to a previously reported parent compound $Rb_2Mn_3(VO_4)_2CO_3$,[25,26] and like the parent compound, can be grown as large high quality single crystals using a high temperature hydrothermal process. Despite their structural similarities the two new compounds crystallize in different space groups. Structure **I** forms in the trigonal space group $P\bar{3}1c$, while **II** crystallizes in the hexagonal space group $P6_3/m$, and is isostructural to the original vanadate carbonate, $Rb_2Mn_3(VO_4)_2CO_3$. DFT calculations correlate the structural stability of the compounds in their respective space groups. The calculations suggested for example that the rubidium containing compound would have carbonate bond distances that would be too short in the hexagonal structure and we propose that this is one of the driving forces for its lower symmetry.

Detailed magnetic studies of $Rb_2Mn_3(VO_4)CO_3$ (**I**) show complex magnetic behavior, generally similar to that of the parent $K_2Mn_3(VO_4)CO_3$ despite its lower symmetry. This is not so surprising since the symmetry reduction occurs because of the behavior of the non-magnetic cations and oxyanions in the structure. It exhibits three antiferromagnetic transitions, at T_N = 77 K, 2.3 K, and 1.5 K. For the higher temperature transition, the Mn spins arrange antiparallel within the plane, and ferromagnetically across the *c*-axis. The lower temperature spin structure has either a collinear or canted magnetic structure for the triangular Mn lattice, as indicated by single crystal neutron diffraction data. In contrast, the cobalt analog, **II**, displays considerably different magnetic data, having easy plane anisotropy, *versus* easy axis anisotropy in **I**. Compound **II** has two linear Curie Weiss regions between room temperature and 8 K, with an inflection region between 150 and 50 K. Both linear regions have negative Curie Weiss values suggesting antiferromagnetic ordering, and like many Co^{2+} ions, displays magnetic susceptibility values greater than ideal spin only values. These values suggest unusually large spin-order coupling for a first row transition metal. Below 8 K the compound displays complex magnetic behavior that is highly anisotropic as might be expected for a structure containing two complex layers. Single crystal neutron diffraction measurements are underway to determine the magnetic structures of this novel cobalt compound. It is clear that the combination of tetrahedral $(VO_4)^{3-}$ and trigonal planar $(CO_3)^{2-}$ building blocks with open shell transition metal ions is a rich source of new magnetically complex materials.

Conflicts of interest

There are no conflicts to declare.

Acknowledgements

We are indcebted to the National Science Foundation NSF-DMR-1808371 and NSF-OIA-1655740 for financial support of the synthesis, crystal growth, and DFT work. Magnetic work

was performed in the Materials Science and Engineering Division (MSTD) and Spallation Neutron Source (SNS) in Oak Ridge National Laboratory partly supported by the U.S. Department of Energy (DOE), Office of Science, Basic Energy Sciences (BES) and by the Scientific User Facilities Division, Basic Energy Sciences, U.S. Department of Energy (DOE), respectively. Simulations were performed on the Palmetto Supercomputer Cluster, which is maintained by the Cyberinfrastructure Technology Integration Group at Clemson University.

Notes and references

1 W. L. Queen, J. P. West, S.-J. Hwu, D. G. VanDerveer, M. C. Zarzyczny and R. A. Pavlick, *Angew. Chem., Int. Ed.*, 2008, **47**, 3791–3794.
2 J. Livage, *Coord. Chem. Rev.*, 1998, **178–180**(Part 2), 999–1018.
3 N. Wang, Z. He, M. Cui, W. Guo, S. Zhang and M. Yang, *Cryst. Growth Des.*, 2015, **15**, 1619–1624.
4 X. Wang, Z. Liu, A. Ambrosini, A. Maignan, C. L. Stern, K. R. Poeppelmeier and V. P. Dravid, *Solid State Sci.*, 1998, **2**, 99–107.
5 L. D. Sanjeewa, M. A. McGuire, V. O. Garlea, L. Hu, G. Chumanov, C. D. McMillen and J. W. Kolis, *Inorg. Chem.*, 2015, **54**, 7014–7020.
6 L. D. Sanjeewa, M. A. McGuire, C. D. McMillen, V. O. Garlea and J. W. Kolis, *Chem. Mater.*, 2017, **29**, 1404–1412.
7 L. D. Sanjeewa, C. D. McMillen, D. Willett, G. Chumanov and J. W. Kolis, *J. Solid State Chem.*, 2016, **236**, 61–68.
8 T. M. Smith Pellizzeri, C. D. McMillen, S. Pellizzeri, Y. Wen, R. B. Getman, G. Chumanov and J. W. Kolis, *J. Solid State Chem.*, 2017, **255**, 225–233.
9 O. Clemens, J. Rohrer and G. Nénert, *Dalton Trans.*, 2016, **45**, 156–171.
10 L. D. Sanjeewa, M. A. McGuire, C. D. McMillen, D. Willett, G. Chumanov and J. W. Kolis, *Inorg. Chem.*, 2016, **55**, 9240–9249.
11 K. Sun, A. P. Litvinchuk, J. Tapp, B. Lorenz and A. Möller, *Inorg. Chem.*, 2015, **54**, 898–904.
12 N. Bellido, C. Martin, C. Simon and A. Maignan, *J. Phys.: Condens. Matter*, 2007, **19**, 056001.
13 G. Lawes, A. B. Harris, T. Kimura, N. Rogado, R. J. Cava, A. Aharony, O. Entin-Wohlman, T. Yildirim, M. Kenzelmann, C. Broholm and A. P. Ramirez, *Phys. Rev. Lett.*, 2005, **95**, 087205.
14 D. E. Freedman, R. Chisnell, T. M. McQueen, Y. S. Lee, C. Payen and D. G. Nocera, *Chem. Commun.*, 2011, **48**, 64–66.
15 K. G. S. Ranmohotti, W. L. Queen, J. P. West, D. VanDerveer and S.-J. Hwu, *J. Chem. Crystallogr.*, 2009, **39**, 303–307.
16 D. E. Bugaris and H.-C. zur Loye, *Angew. Chem., Int. Ed.*, 2012, **51**, 3780–3811.
17 J. Gao, J. Li, D. Sulejmanovic and S.-J. Hwu, *Inorg. Chem.*, 2015, **54**, 1136–1144.
18 S. Erdei, *J. Cryst. Growth*, 1993, **134**, 1–13.
19 C. D. McMillen and J. W. Kolis, *Dalton Trans.*, 2016, **45**, 2772–2784.
20 T. M. Smith Pellizzeri, C. D. McMillen, Y. Wen, G. Chumanov and J. W. Kolis, *Inorg. Chem.*, 2017, **56**, 4206–4216.
21 T. M. S. Pellizzeri, M. A. McGuire, C. D. McMillen, Y. Wen, G. Chumanov and J. W. Kolis, *Dalton Trans.*, 2018, **47**, 2619–2627.
22 L. D. Sanjeewa, M. A. McGuire, T. M. Smith Pellizzeri, C. D. McMillen, V. Ovidiu Garlea, D. Willett, G. Chumanov and J. W. Kolis, *J. Solid State Chem.*, 2016, **241**, 30–37.
23 L. D. Sanjeewa, V. O. Garlea, M. A. McGuire, C. D. McMillen, H. Cao and J. W. Kolis, *Phys. Rev. B: Condens. Matter Mater. Phys.*, 2016, **93**, 224407.
24 V. O. Garlea, M. A. McGuire, L. D. Sanjeewa, D. M. Pajerowski, F. Ye and J. W. Kolis, *AIP Adv.*, 2018, **8**, 101407.
25 O. V. Yakubovich, E. V. Yakovleva, A. N. Golovanov, A. S. Volkov, O. S. Volkova, E. A. Zvereva, O. V. Dimitrova and A. N. Vasiliev, *Inorg. Chem.*, 2013, **52**, 1538–1543.
26 V. O. Garlea, L. D. Sanjeewa, M. A. McGuire, C. D. Batista, A. M. Samarakoon, D. Graf, B. Winn, F. Ye, C. Hoffmann and J. W. Kolis, *Phys. Rev. X*, 2019, **9**, 011038.
27 K. A. Ross, J. M. Brown, R. J. Cava, J. W. Krizan, S. E. Nagler, J. A. Rodriguez-Rivera and M. B. Stone, *Phys. Rev. B: Condens. Matter Mater. Phys.*, 2017, **95**, 144414.
28 *Apex 3*, Bruker-AXS Inc., Madison, WI.
29 G. M. Sheldrick, *Acta Crystallogr., Sect. A: Found. Crystallogr.*, 2008, **64**, 112–122.
30 P. Giannozzi, S. Baroni, N. Bonini, M. Calandra, R. Car, C. Cavazzoni, D. Ceresoli, G. L. Chiarotti, M. Cococcioni, I. Dabo, A. D. Corso, S. de Gironcoli, S. Fabris, G. Fratesi, R. Gebauer, U. Gerstmann, C. Gougoussis, A. Kokalj, M. Lazzeri, L. Martin-Samos, N. Marzari, F. Mauri, R. Mazzarello, S. Paolini, A. Pasquarello, L. Paulatto, C. Sbraccia, S. Scandolo, G. Sclauzero, A. P. Seitsonen, A. Smogunov, P. Umari and R. M. Wentzcovitch, *J. Phys.: Condens. Matter*, 2009, **21**, 395502.
31 P. Giannozzi, O. Andreussi, T. Brumme, O. Bunau, M. B. Nardelli, M. Calandra, R. Car, C. Cavazzoni, D. Ceresoli, M. Cococcioni, N. Colonna, I. Carnimeo, A. D. Corso, S. de Gironcoli, P. Delugas, R. A. DiStasio, A. Ferretti, A. Floris, G. Fratesi, G. Fugallo, R. Gebauer, U. Gerstmann, F. Giustino, T. Gorni, J. Jia, M. Kawamura, H.-Y. Ko, A. Kokalj, E. Küçükbenli, M. Lazzeri, M. Marsili, N. Marzari, F. Mauri, N. L. Nguyen, H.-V. Nguyen, A. Otero-de-la-Roza, L. Paulatto, S. Poncé, D. Rocca, R. Sabatini, B. Santra, M. Schlipf, A. P. Seitsonen, A. Smogunov, I. Timrov, T. Thonhauser, P. Umari, N. Vast, X. Wu and S. Baroni, *J. Phys.: Condens. Matter*, 2017, **29**, 465901.
32 J. P. Perdew, K. Burke and M. Ernzerhof, *Phys. Rev. Lett.*, 1996, **77**, 3865–3868.
33 G. Prandini, A. Marrazzo, I. E. Castelli, N. Mounet and N. Marzari, *npj Comput. Mater.*, 2018, **4**, 1–13.
34 K. Lejaeghere, G. Bihlmayer, T. Björkman, P. Blaha, S. Blügel, V. Blum, D. Caliste, I. E. Castelli, S. J. Clark, A. D. Corso, S. de Gironcoli, T. Deutsch, J. K. Dewhurst,

I. D. Marco, C. Draxl, M. Dułak, O. Eriksson, J. A. Flores-Livas, K. F. Garrity, L. Genovese, P. Giannozzi, M. Giantomassi, S. Goedecker, X. Gonze, O. Grånäs, E. K. U. Gross, A. Gulans, F. Gygi, D. R. Hamann, P. J. Hasnip, N. a. W. Holzwarth, D. Iuşan, D. B. Jochym, F. Jollet, D. Jones, G. Kresse, K. Koepernik, E. Küçükbenli, Y. O. Kvashnin, I. L. M. Locht, S. Lubeck, M. Marsman, N. Marzari, U. Nitzsche, L. Nordström, T. Ozaki, L. Paulatto, C. J. Pickard, W. Poelmans, M. I. J. Probert, K. Refson, M. Richter, G.-M. Rignanese, S. Saha, M. Scheffler, M. Schlipf, K. Schwarz, S. Sharma, F. Tavazza, P. Thunström, A. Tkatchenko, M. Torrent, D. Vanderbilt, M. J. van Setten, V. V. Speybroeck, J. M. Wills, J. R. Yates, G.-X. Zhang and S. Cottenier, *Science*, 2016, **351**, aad3000.

35 M. Cococcioni and S. de Gironcoli, *Phys. Rev. B: Condens. Matter Mater. Phys.*, 2005, **71**, 035105.

36 A. Jain, G. Hautier, S. P. Ong, C. J. Moore, C. C. Fischer, K. A. Persson and G. Ceder, *Phys. Rev. B: Condens. Matter Mater. Phys.*, 2011, **84**, 045115.

37 F. Ye, Y. Liu, R. Whitfield, R. Osborn and S. Rosenkranz, *J. Appl. Crystallogr.*, 2018, **51**, 315–322.

38 T. Susuki, N. Kurita, T. Tanaka, H. Nojiri, A. Matsuo, K. Kindo and H. Tanaka, *Phys. Rev. Lett.*, 2013, **110**, 267201.

39 Y. Kamiya, L. Ge, T. Hong, Y. Qiu, D. L. Quintero-Castro, Z. Lu, H. B. Cao, M. Matsuda, E. S. Choi, C. D. Batista, M. Mourigal, H. D. Zhou and J. Ma, *Nat. Commun.*, 2018, **9**, 1–11.

40 K. Okhotnikov, T. Charpentier and S. Cadars, *J. Cheminf.*, 2016, **8**, 17.

41 F. E. Mabbs and D. J. Machin, *Magnetism and Transition Metal Complexes*, Courier Corporation, 2008.

42 B. N. Figgis and M. A. Hitchman, *Ligand Field Theory and Its Applications*, Wiley-VCH, 2000.

43 R. Rawl, M. Lee, E. S. Choi, G. Li, K. W. Chen, R. Baumbach, C. R. dela Cruz, J. Ma and H. D. Zhou, *Phys. Rev. B: Condens. Matter Mater. Phys.*, 2017, **95**, 174438.

44 G. Nakayama, S. Hara, H. Sato, Y. Narumi and H. Nojiri, *J. Phys.: Condens. Matter*, 2013, **25**, 116003.

45 J. L. Her, C. C. Chou, Y. H. Matsuda, K. Kindo, H. Berger, K. F. Tseng, C. W. Wang, W. H. Li and H. D. Yang, *Phys. Rev. B: Condens. Matter Mater. Phys.*, 2011, **84**, 235123.